Published by IOP Publishing for Sissa Medialab

Received: *June 19, 2025*
Accepted: *July 28, 2025*
Published: *August 29, 2025*

The HERD calorimeter: prototype response to high energy nuclei

O. Adriani,[a,b] **G. Ambrosi,**[c] **M. Antonelli,**[d] **Y. Bai,**[e] **X. Bai,**[e] **T. Bao,**[f] **M. Barbanera,**[c] **E. Berti,**[b] **P. Betti,**[b] **G. Bigongiari,**[g,h] **M. Bongi,**[a,b] **V. Bonvicini,**[d] **S. Bottai**[b,*] **W. Cao,**[e] **J. Casaus,**[m] **D. Cerasole,**[n,o] **Z. Chen,**[e] **X. Cui,**[f] **R. D'Alessandro,**[a,b] **I. De Mitri,**[i,l] **S. Detti,**[b] **A. Di Giovanni,**[i,l] **L. Di Venere,**[o] **C. Diaz,**[m] **Y. Dong,**[f] **M. Duranti,**[c] **F. Gargano,**[o] **J. Gao,**[e] **S. Guo,**[f] **F. Giovacchini,**[m] **N. Finetti,**[p,b] **V. Formato,**[q] **Y. Jiang,**[r,c] **X. Liang,**[e] **R. Li,**[e] **C. Liao,**[f] **X. Liu,**[f] **L. Lyu,**[e] **J. Marin,**[m] **G. Martinez,**[m] **N. Mori,**[b] **A. Oliva,**[s] **L. Pacini,**[b] **P. Papini,**[b] **R. Pillera,**[o] **C. Pizzolotto,**[d] **Z Quan,**[f] **J.J. Qin,**[e] **M. Scaringella,**[b] **D. Serini,**[o] **D. Shi,**[e] **G. Silvestre,**[c] **O. Starodubtsev,**[b] **X. Tang,**[f] **A. Tiberio,**[b] **E. Vannuccini,**[b] **M. Velasco,**[m] **B. Wang,**[e] **J. Wang,**[f] **R. Wang,**[f] **Z. Wang,**[f] **M. Xu,**[f] **X. Yang,**[f] **G. Zampa,**[d] **N. Zampa,**[d] **S. Zhang**[f] **and J. Zheng**[e]

[a] *Department of Physics and Astronomy, University of Florence, 50019 Sesto Fiorentino, Florence, Italy*
[b] *INFN, Sezione di Firenze, 50019 Sesto Fiorentino, Florence, Italy*
[c] *INFN, Sezione di Perugia, 06100 Perugia, Italy*
[d] *INFN, Sezione di Trieste, Padriciano 99, 34149 Trieste, Italy*
[e] *Xi'an Institute of Optics and Precision Mechanics, Chinese Academy of Sciences, 710119, Xi'an, China*
[f] *Institute of High Energy Physics, Chinese Academy of Sciences, 100049, Beijing, China*
[g] *Department of Physical Sciences, Earth and Environment, University of Siena, 53100 Siena, Italy*
[h] *INFN, Sezione di Pisa, Largo B. Pontecorvo, 3, 56127 Pisa, Italy*
[i] *Gran Sasso Science Institute (GSSI), Viale Crispi 7, 67100 L'Aquila , Italy*
[l] *INFN, Laboratori Nazionali del Gran Sasso, Via Acitelli 22, 67100 Assergi, L'Aquila, Italy*
[m] *Centro de Investigaciones Energéticas, Medioambientales y Tecnológicas (CIEMAT), 28040 Madrid, Spain*
[n] *Dipartimento Interateneo di Fisica "M. Merlin" dell'Università e del Politecnico di Bari, 70126 Bari, Italy*
[o] *Istituto Nazionale di Fisica Nucleare (INFN) — Sezione di Bari, 70126 Bari, Italy*
[p] *Department of Physical and Chemical Sciences, University of L'Aquila, Via Vetoio, Coppito, 67100 L'Aquila, Italy*
[q] *INFN, Sezione di Roma Tor Vergata, 00133 Roma, Italy*
[r] *Università degli Studi di Perugia, 06100 Perugia, Italy*
[s] *INFN, Sezione di Bologna, 40126 Bologna, Italy*

E-mail: bottai@fi.infn.it

[*] Corresponding author.

https://doi.org/10.1088/1748-0221/20/08/P08034

Abstract: HERD is a space-borne calorimetric experiment that aims to extend current direct measurements of cosmic rays to the PeV energy range. The main feature of the instrument is its ability to measure particles coming from all directions, with the main detector being a deep, homogeneous 3D calorimeter. A large prototype of the calorimeter was tested at CERN in 2023 as part of an extensive beam test campaign. This paper describes the data analysis and performance of the calorimeter prototype for high-energy nuclei. Several important information and parameters for the calibration of the HERD calorimeter are reported.

Keywords: Calorimeters; Large detector systems for particle and astroparticle physics; Particle detectors; Ion identification systems

2025 JINST 20 P08034

Contents

1 The HERD mission

Recent experiments dedicated to direct measurements of cosmic rays (CR) have made numerous observations that have led to the discovery of several unexpected features in CR spectra [1]. These results have significantly improved our understanding of CR acceleration and propagation. Although these experiments have provided excellent information on CR physics, the energy range of current space experiments is limited. For example, the AMS-02 [2] spectrometer Maximum Detectable Rigidity is a few TV, while the limited acceptance of space calorimeters like CALET [3] and DAMPE [4] allows for the observation of particles up to a few hundred TeV per nucleon.

The High Energy cosmic-Radiation Detection (HERD) project [5, 6] is a space-based experiment scheduled to be installed on the Chinese Space Station (CSS) around 2027. This initiative is a partnership between various Chinese and European academic and research institutions. With its innovative design, HERD will push the boundaries of CR spectrum direct measurements into regions previously unexplored by space-based instruments. The experiment aims to detect protons and nuclei up to the PeV region, where a change in the spectral index of the total particle spectrum is observed with ground experiments. These ground detectors perform indirect measurements of CR by exploiting their interaction with the Earth's atmosphere. As a result, they suffer from significant systematic errors and are unable to distinguish unambiguously the charge of the different incoming particles. Furthermore, HERD will make the first direct observation of the electron+positron flux up to tens of TeV, it will measure the photon spectrum ranging from 500 MeV to 100 TeV and it will also monitor the gamma-ray sky with a wide field of view [7].

To achieve the HERD's goals, a large acceptance is required, so the experiment is designed to correctly reconstruct particles entering the detector from each side, in contrast to typical CR experiments, which are usually designed like telescopes and only accept particles coming from the top side. This innovative design was first studied in detail by the CaloCube R&D project [8–10] and then adapted and improved by the HERD collaboration. An image of the possible design of the detector is shown in figure 1. HERD consists of several sub-detectors: starting from the outside, Silicon Charge Detectors (SCD) [11], Plastic Scintillator Detectors (PSD) [12–14], and Fiber Trackers (FIT) [15] are

2025 JINST 20 P08034

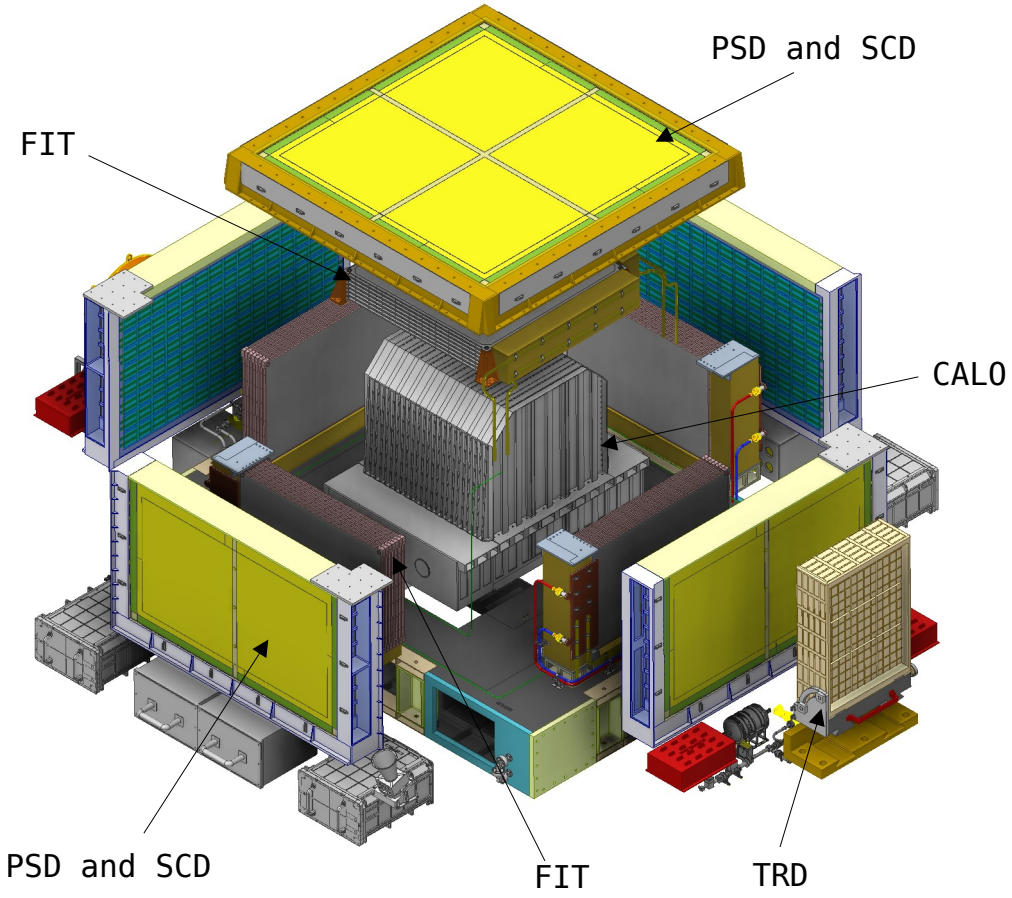

Figure 1. Expanded 3D image of HERD: the arrows indicate some of the sub detectors.

present on each detector face, excluding the bottom one. These detectors reconstruct the absolute value of particle charge and particle directions, and allow gamma-ray observation [7]. Furthermore, on a single lateral face, a small Transition Radiation Detector (TRD) [16] is present; this provides an independent measurement of TeV proton and GeV electron primary energy.

The core of the instrument is the calorimeter (CALO): it is briefly described in the next section while details about the expected performance of this sub-detector are well described in ref. [17].

2 The HERD calorimeter and its large prototype

The HERD CALO will consists of about 7500 cubic scintillating crystals, $3 \times 3 \times 3\,\mathrm{cm}^3$, made of Lutetium-yttrium oxyorthosilicate (LYSO). This material has been selected among other scintillators due to its good light yield and high density, which significantly improve the CALO performance for protons and nuclei. A detailed comparison of calorimeter performance made of different materials is well described in ref. [8]. The 3 cm side length of a single LYSO cube corresponds to 0.14 interaction length λ_i, 2.73 radiation length X_0, and to an amount of traversed material of $21.75\,\mathrm{g/cm}^2$. The design is also compliant with the requirements of the HERD mission: a weight of about 4 metric tons, a maximum volume of a few m^3, and a maximum power consumption of 1.5 kW. The total depth of

2025 JINST 20 P08034

Table 1. PD parameters for a bias voltage of about 50 V.

Part number	Active area	Junction cap.	Dark current	Response @ 420 nm	Rise time
Large PD	25 mm^2	< 30 pF	< 0.2 nA	~ 0.15 A/W	~ 15 ns
Small PD	1.6 mm^2	< 6 pF	< 7 nA	~ 0.2 A/W	~ 15 ns

the CALO for vertical particles is about 55 radiation lengths and about 3 proton interaction lengths. This allows for total absorption of electromagnetic showers up to tens of TeV and a high interaction probability for protons and nuclei.

The effective geometric factor is better than 2 m^2sr for electrons and 1 m^2sr for protons and nuclei [17]. The energy resolution at 10 TeV is about 2% for electrons, 30% for protons, and 22% for carbon nuclei. Thanks to the 3D sampling of the shower, electrons are clearly separated from the proton background: the residual proton contamination is a few percent up to the 10 TeV region. By reconstructing the shower using only the CALO, the shower axis is identified with an angular resolution better than one degree for TeV particles.

The HERD collaboration is assessing the feasibility of reading out the LYSO cubes with two independent systems: the advantages of having this "double read-out system" are described in ref. [18] and [19]. In summary, two systems will decrease the systematic errors related to the energy scale calibration. The first system [19] is based on Wavelength Shifter Fibers (WLF) connected to Intensified scientific CMOS. The second one is used for acquiring the data discussed in this paper: the details of the system configuration are reported in ref. [18, 20, 21]. This system consists of photo-diodes (PDs) coupled with custom front-end electronics: this configuration was first studied and validated by the CaloCube collaboration [9, 22]. A custom sensor is glued to each LYSO cube. The scintillation light detector consists of two PDs with different active areas assembled in a monolithic package, developed by INFN in collaboration with Excelitas Technologies. The large area PD (LPD) detects small energy deposits in LYSO while the small one (SPD) detects high signals. Table 1 includes important parameters of the PDs. The SPD active area is covered by an optical filter with a transmission of about 5% at the LYSO wavelength ($\sim$ 420 nm) in order to further increase the LPD/SPD signal ratio. The main component of the front-end electronics is the HiDRA3.0 chip, which is an updated version of the CASIS [23] chip. Thanks to the unique design of a double-gain charge-sensitive amplifier, HiDRA features low noise (about 2500 equivalent electrons), low power consumption (3.75 mW/channel), and a large dynamic range (from a few fC to 52.6 pC). The chip also has self-trigger capabilities and anti-saturation circuitry. Custom kapton cables are used to connect each PD to a dedicated HiDRA channel.

To evaluate the HERD CALO performance and calibrate its response to high-energy beams, a prototype calorimeter composed of $7 \times 7 \times 21$ LYSO crystals was assembled during 2023. All the crystals are equipped with both read-out systems, i.e., WLF and PDs. The 3D design and two images of the prototype are shown in figure 2 and 3, respectively. The PDs are connected to the front-end boards with custom kapton cables accurately designed for the HERD experiment [18]. The main components of the front-end boards are: 12 HiDRA (version 3) chips, 3 ADC chips, and 1 FPGA. Finally, a back-end board is assembled on top of the CALO. The main goals of this board are to acquire data from the front-end, handle the fast trigger information, communicate with the main PC, and configure the front-end parameters for the current acquisition run.

2025 JINST 20 P08034

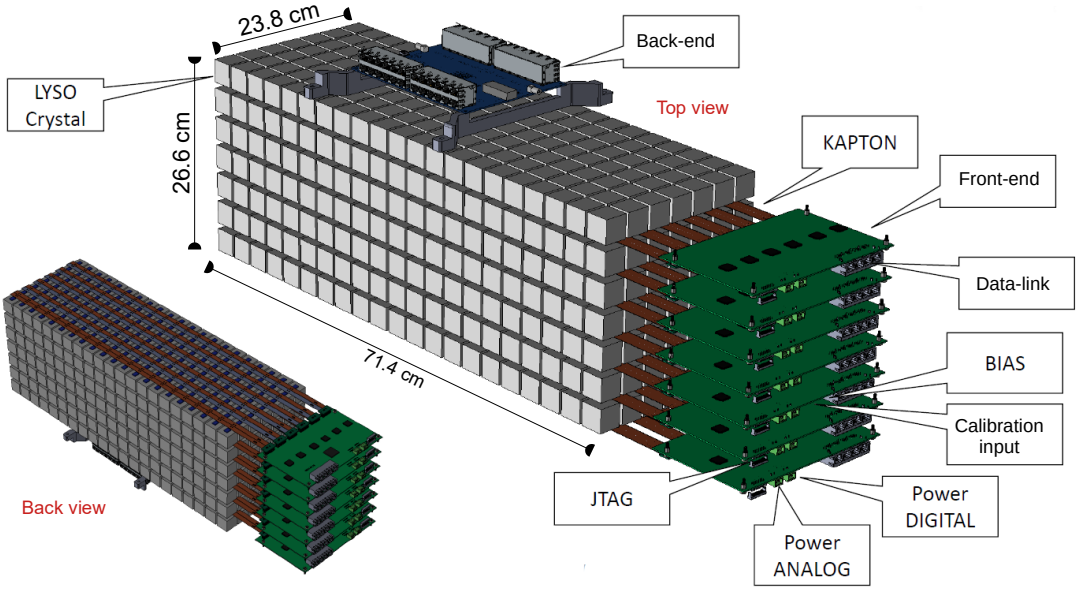

Figure 2. Mechanical design of the prototype main components, LYSO crystals, back-end board, front-end boards and kapton cables.

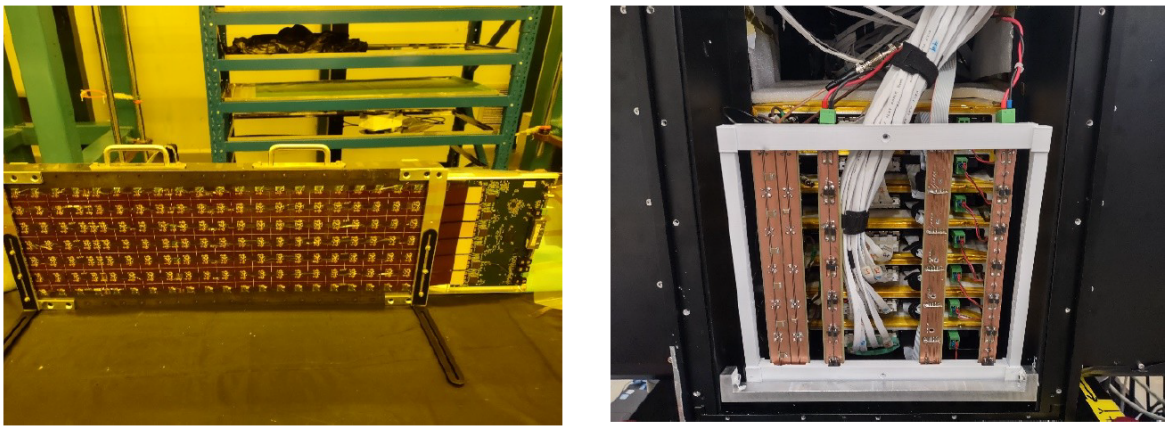

Figure 3. Photographs of the bottom face of a horizontal 7x21 layer (here disposed in vertical position) and the back of the CALO, where the readout and power cables are connected to front-end boards.

3 The beam test campaign

The prototype described in the previous section and several other HERD sub-detectors were tested during an extensive campaign at CERN with PS (east area, EA) and SPS (north area, NA) secondary beams. In this paper, we will present the results obtained with high-energy nuclei acquired in the NA. The beam consists of ions produced by the fragmentation of a ^{129}Xe primary beam of 150 GeV/A kinetic energy hitting a 40 mm Be target. A magnetic spectrometer placed downstream the interaction point allows to select fragments with 330 GV magnetic rigidity ($R = pc/Ze$).

Several sub-detectors were placed in front of the CALO, including different prototypes of PSD, SCD, FIT, a trigger box made of plastic scintillator, and an additional charge detector named Charge

2025 JINST 20 P08034

Tagger [24] used for heavy ion tagging. The Charge Tagger consists of 6 photo-diodes, each one featuring a $9.2 \times 9.2\,\mathrm{mm}^2$ active area. The photo-diodes are mounted one above the other along the beam direction and perpendicular to it, so that the particles cross all of them. The PDs are blinded and measure the ionization induced by charged particles within the diode itself. The Charge Tagger is positioned in front of the CALO at a distance of 16.6 cm along the beam direction. The CALO and the Charge Tagger are aligned so that the beam first crosses the Charge Tagger and then enters the CALO exactly in the center of the central cube of its 7×7 face. The beam path then continues along the central axis of the CALO traversing 21 layers of 7×7 cube each. For the analysis described in this paper, data from Charge Tagger and CALO (read-out by PDs system) were employed to determine the particle charge and analyze the calorimeter response.

4 Data analysis

The analysis of muon data acquired in the EA and its use for calibration is described in [25]. The data of high-energy nuclei acquired in the NA have been analyzed in three subsequent steps. First the different nuclei are discriminated, then the first nuclear interaction point in the CALO is determined and lastly the correlation between the energy deposited in the CALO and the position of the interaction point is studied.

4.1 Charge discrimination

The energy deposited in each PD of the Charge Tagger by non interacting ions is due to ionization and is expected to scale with Z^2 where Z is the charge expressed in atomic number. The data analysis of the Charge Tagger follows the subsequent scheme:

- Signal amplitude evaluation in ADC for each of the six PDs, ensuring it exceeded three times the noise threshold.
- Signal conversion from ADC to Minimum Ionizing Particle (MIP) units using prior calibration. The conversion parameters from ADC to MIP were obtained for each PD by analysing the carbon peak in the fragmented SPS beam.
- Conversion of the signal from MIP to atomic number (Z).
- Consistency of all the six PDs signals is requested and the mean value calculated. The consistency requirement is defined as a signal difference of less than 1.5 charge units.

Figure 4 is reports the correlation of the Charge Tagger signal with the energy deposited in the CALO entrance cube (First Cube). The clusters due to the ionization signals of non-interacting nuclei are clearly visible. The events with high energy release in the first cube when the Charge Tagger signal is $Z \leq 2$ are probably due to ions interacting before the Charge Tagger. By requesting consistency between the Charge Tagger and the First Cube ionization signals, ions with Z ranging from 2 to 14 that do not interact in the first cube are resolved very well with negligible contamination. For Z greater than 14, the low statistics do not allow for clean identification, so these nuclei are not considered in this paper.

2025 JINST 20 P08034

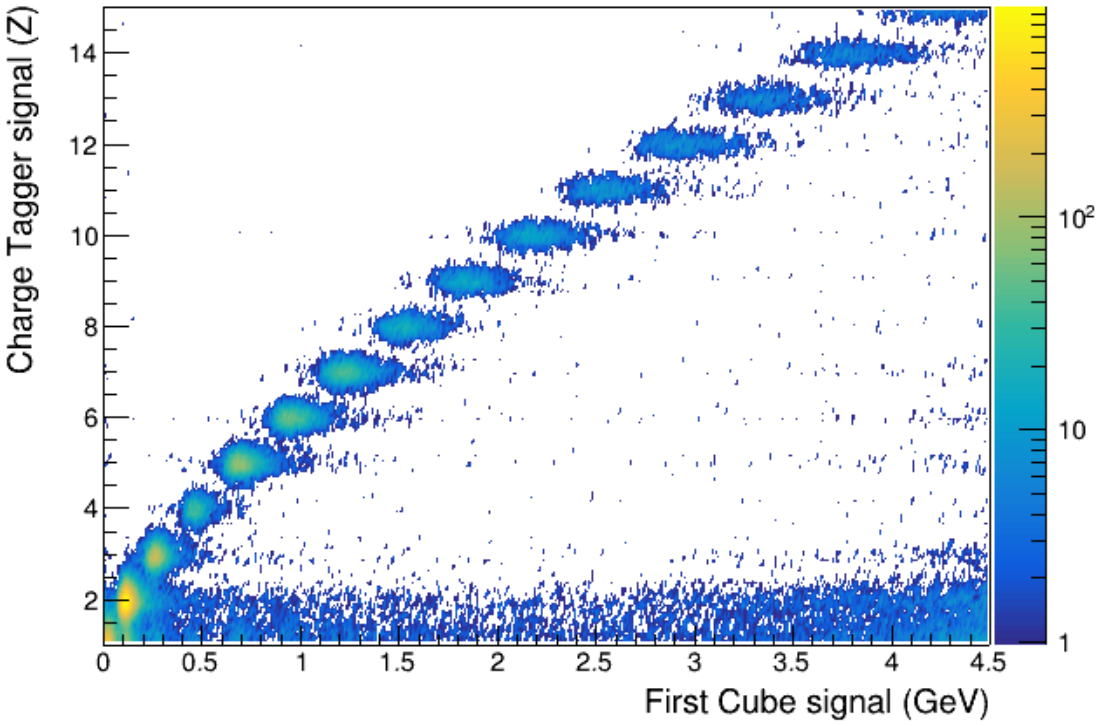

Figure 4. Scatter plot of Charge Tagger signal versus energy deposited in the First cube.

4.2 Determination of first nuclear interaction

Since the First Cube is used for charge selection of non-interacting ions, the events selected for the analysis are those whose nuclear interactions occur in the second layer or even deeper inside the CALO. Once the first nuclear inelastic interaction (here simply called "first interaction") occurs, it fragments the nucleus, secondaries are produced and a hadronic shower begins to dissipate the ion energy in the CALO. The deeper the position of the first interaction, the less material remains for the shower to develop and the less energy is deposited in the CALO. For this reason, a correct energy reconstruction must take into account the actual position of the first nuclear interaction that gives rise to the hadronic shower. The point of first interaction is reconstructed by looking at the first cube above a certain threshold among those belonging to the central column of 21 cubes through which the beam passes. Starting from the entrance of the beam into the CALO, if a cube with signal above the threshold is found and the successive neighbouring cube has an even greater signal, the center of this former cube is taken as the point of first interaction. In order to determine the value of the threshold to be used for each nuclear species, we look at the correlation between the signal of two adjacent cubes in the column when no interaction has occurred before, for example the second cube (Cube 2) in the column versus the third (Cube 3). Figure 5 shows the correlation for Carbon. The cluster around 1 GeV corresponds to ionization release without interaction in both cubes while higher signals outside the blob indicate the presence of a nuclear interaction happened in the cube or before it. However, the figure is not symmetrical with respect to the two cubes, since if there is an interaction in Cube 2, Cube 3 must also be involved, whereas if there is no interaction in Cube 2, Cube 3 can have

2025 JINST 20 P08034

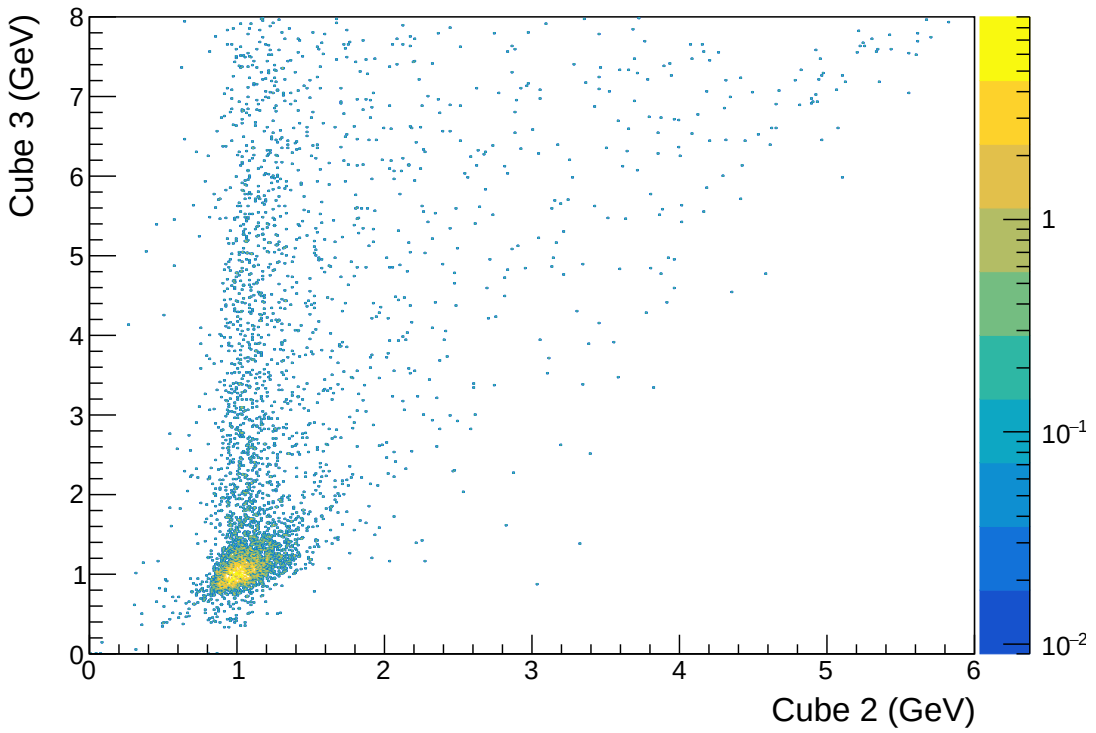

Figure 5. Scatter plot of Cube 2 signal versus Cube 3 signal for Carbon (see text).

both typical ionization or interaction signals. Moreover, we can conclude that the lower threshold for interaction in Cube 2 should be the smaller of the values that select events without signals in the ionization region for both Cube 2 and Cube 3. For carbon, this value is around 1.5 GeV. Such a value, determined for Cube 2, can be generalized to hold for any cube in case no interaction has been found before it in the central column, and thus be used in the proposed algorithm for determining the point of first interaction. For each nuclear species the same procedure is applied to determine the threshold. The point of first interaction has been determined for each shower event and some results are reported in figure 6 for what concerns the distribution of such variable. The validation of the methodology and the thresholds is done by Monte Carlo simulation [8] and "a posteriori" based on the correct behavior of the resulting probability distribution, which must be well represented by an exponential law. Deviations from the expected exponential distribution, mainly for the first cube, are indeed observed when the thresholds are varied with respect to the reference values (figure 6).

4.3 Analysis of energy deposition

Even if showers begin in the second 7×7 cube layer, the depth of the calorimeter ($\approx 2.8\ \lambda_i$ for 20 layers) is not enough for complete containment. Figure 7 shows the average shower profile measured for nuclei interacting in the second layer and clearly shows the presence of longitudinal energy leakage. In contrast, the lateral profiles of the showers in figure 7 show quite good lateral containment. The outer lateral shell contains about 5% of the total energy released, and the steep trend of the profiles suggests that the lateral energy leakage is less than 5%. The longitudinal energy leakage will also

2025 JINST 20 P08034

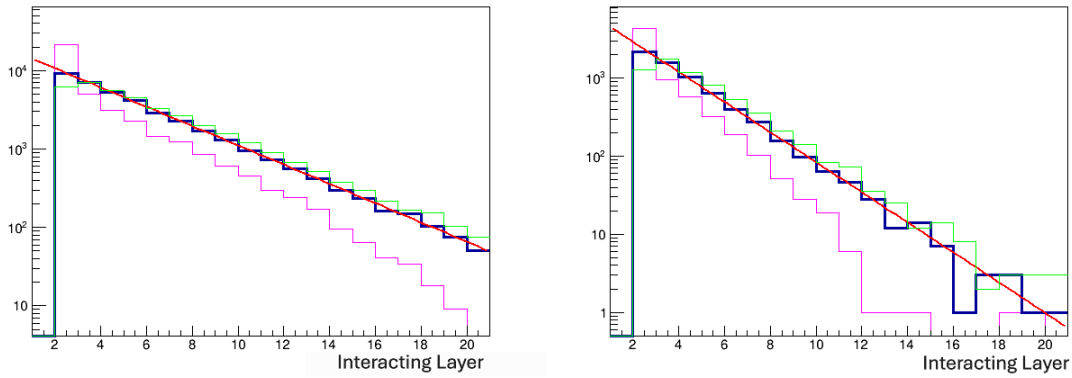

Figure 6. Distribution of layers where the point of first interaction occurs. The layers are numbered from the entrance to the end of the CALO. One layer corresponds to 3 cm (21.75 g/cm^2) of LYSO. The left figure is for Helium and the right figure is for Carbon. The blue distributions, fitted by an exponential law, are for reference values of the thresholds. The distributions in magenta are obtained by scaling the threshold by a factor of 0.7, while those in green are scaled by a factor of 1.6. The interaction length obtained by fitting the distributions is 3.53 layers for Helium and 2.27 layers for Carbon.

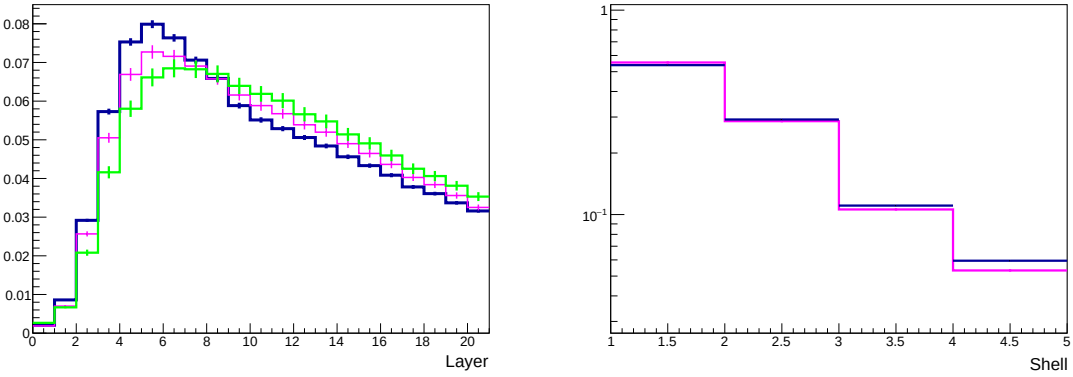

Figure 7. The left figure shows the normalized distribution of the average energy deposited in the subsequent layers of CALO for showers initiated in the second layer. The blue histogram is for $Z = 2$, the magenta histogram is for $Z = 6$, and the green histogram is for $Z = 14$. The right figure shows the normalized distribution of the average energy deposited in the shells of cubes surrounding the central column. The shell 1 corresponds to the sum of the cubes of the central column, the shell 2 corresponds to the sum of the cubes adjacent to the central column, the other shells follow the same criteria going towards the outer part of the CALO. The blue histogram is for $Z = 2$ and the magenta histogram is for $Z = 6$. The result for $Z = 14$ follows exactly the same distribution and is omitted. All histograms are normalized to show a unit integral.

affect the detection of cosmic ray nuclei in the full HERD calorimeter. In this context, since the calorimeter aims to detect particles coming from all directions, many nuclei will, for geometrical reasons, cross an amount of LYSO that is considerably less than the maximum depth of $\approx 3\lambda_i$. Since the HERD calorimeter allows the determination of the shower axis and the point of first interaction, this information can be used to infer the energy of the nucleus using the appropriate average ratio of energy released in the CALO to the true energy of the particle [8]. Such a ratio, which is expected to vary with the *effective length* (the distance from the point of first interaction to the end of the

2025 JINST 20 P08034

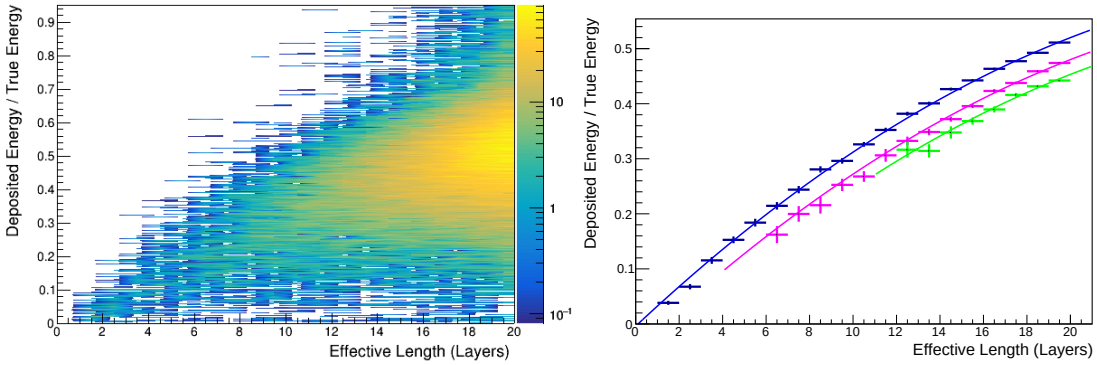

Figure 8. The left figure shows for Helium the scatter plot of the ratio between the deposited energy and the true energy versus the *effective length* measured in layers of LYSO cubes. To convert to other units, keep in mind that one layer corresponds to 3 cm (21.75 g/cm^2) of LYSO. The right figure shows the average value of the same ratio as a function of the *effective length* (see text). The blue points refer to $Z = 2$, the magenta points to $Z = 5$ and the green points to $Z = 11$. The points are fitted with a second degree polynomial; for $Z = 5$ and $Z = 11$ only the zero degree term is varied to fit the points, while the other two terms are fixed to the results obtained for $Z = 2$.

CALO), can be calibrated for each nucleus using Monte Carlo simulations and data analysis from test beam campaigns. A fraction of the events in the HERD experiment will also pass through a TRD, allowing for in-flight calibration.

In figure 8 the total energy detected in the prototype CALO (normalized to the true energy of the nucleus) is plotted against the *effective length* for Helium in the form of a scatter plot for all events. For the maximum value of the *effective length*, the average value of the energy deposited in the CALO (and thus detected as the sum of the signal of all cubes) corresponds to about 50% of the true energy of the nucleus. Part of the total missing energy is due to the "invisible energy" (always present in hadronic showers) and part to the longitudinal leakage of the showers. As the *effective length* decreases, the average value of the deposited energy decreases, as expected. The distribution of the values of the *effective length* is here dominated by higher values due to the fact that the depth of the calorimeter traversed by the beam always has the maximum value of 21 LYSO-cubes. The same is not true for HERD CALO, because when uniformly illuminated by cosmic rays, several particles cross only part of it, so the distribution of *effective length* for HERD is expected to be much more populated by small values [8]. However, this does not invalidate the possibility of extrapolating the results of the present test beam to HERD, since the average of the deposited energy for a fixed value of *effective length* is the same for both, as long as the calorimeter composition is the same. The plot on the right hand side of the figure 8 shows the average values of the fraction of true energy deposited in CALO as a function of *effective length* for 3 different nuclei. The trend is very similar for all the nuclei (and energy = $Z \cdot 330$ GeV) considered in this paper, all the dependence can be well approximated by a second degree polynomial $F(x) = a + bx + cx^2$, where x is the *effective length* measured in layers. The polynomial approximation is not motivated by any physical reason and is not valid for unimportant very small *effective length*, but has been adopted for simplicity. For all the nuclei with $Z > 2$ only the zero degree term is varied in the fit, while the other two terms are kept constant. For nuclei with higher Z, the smaller values of the *effective length* are not sufficiently populated and the corresponding

2025 JINST 20 P08034

points are not used for the fits. As a consequence, for each nucleus, only in a limited range of *effective length* values the approximation by the polynomial is validated. The three terms a, b, c of the second degree polynomial, have been fitted to the points relative to Helium (figure 8); the results are $a = -4.1 \cdot 10^{-3} \pm 3 \cdot 10^{-4}$, $b = 3.71 \cdot 10^{-2} \pm 3 \cdot 10^{-4}$ and $c = -5.4 \cdot 10^{-4} \pm 1 \cdot 10^{-5}$. The curves relative to other nuclei have been fitted with the same polynomial, varying only the zero degree term a. The results for all nuclei are reported in table 2, together with the range of *effective length* used in the fit.

Table 2. Fit results for zero degree term a of the polynomial approximation of deposited Energy fraction vs. *effective length* (see text).

Charge (Z)	a	min *effective length*	max *effective length*
2	$-4.1 \cdot 10^{-3} \pm 3 \cdot 10^{-4}$	2 Layers	20 Layers
3	$-2.6 \cdot 10^{-2} \pm 1 \cdot 10^{-3}$	4 Layers	20 Layers
4	$-3.7 \cdot 10^{-2} \pm 2 \cdot 10^{-3}$	7 Layers	20 Layers
5	$-4.4 \cdot 10^{-2} \pm 1 \cdot 10^{-3}$	5 Layers	20 Layers
6	$-4.7 \cdot 10^{-2} \pm 1 \cdot 10^{-3}$	9 Layers	20 Layers
7	$-5.3 \cdot 10^{-2} \pm 1 \cdot 10^{-3}$	10 Layers	20 Layers
8	$-6.0 \cdot 10^{-2} \pm 1.5 \cdot 10^{-3}$	11 Layers	20 Layers
9	$-6.7 \cdot 10^{-2} \pm 1.5 \cdot 10^{-3}$	11 Layers	20 Layers
10	$-6.4 \cdot 10^{-2} \pm 1.5 \cdot 10^{-3}$	11 Layers	20 Layers
11	$-7.0 \cdot 10^{-2} \pm 1.5 \cdot 10^{-3}$	12 Layers	20 Layers
12	$-7.1 \cdot 10^{-2} \pm 1.5 \cdot 10^{-3}$	12 Layers	20 Layers
13	$-8.2 \cdot 10^{-2} \pm 1.5 \cdot 10^{-3}$	13 Layers	20 Layers
14	$-7.7 \cdot 10^{-2} \pm 1.5 \cdot 10^{-3}$	14 Layers	20 Layers

Once the *effective length* dependence of the average deposited energy is known, it can be used to correct the results event by event on the basis of the reconstructed *effective length*.

Figure 9 shows the distribution of the deposited energy with and without the correction. The *effective length* correction here consists in the rescaling of the energy deposited by each event by a factor $\frac{F(20)}{F(\textit{effective length})}$. The correction allows to eliminate the event by event leakage fluctuations due

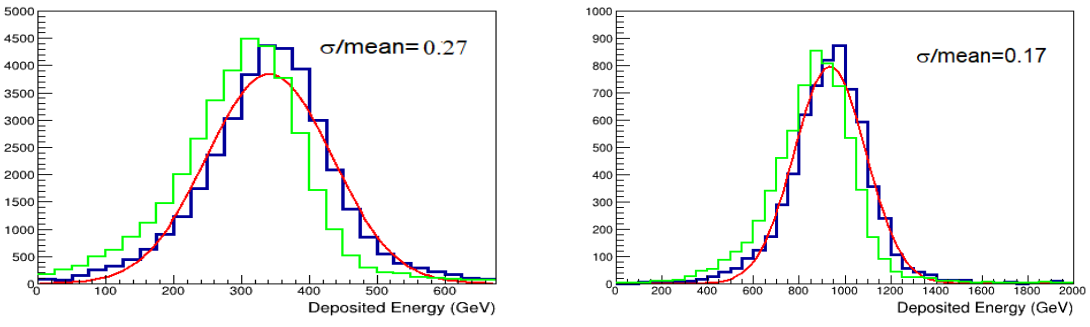

Figure 9. The figures show the distribution of energy deposited and then detected in the calorimeter for Helium (left figure) and Carbon (right figure). The green lines correspond to the energy deposited without the *effective length* correction, while the blue lines include the correction. The red lines show a gaussian fit to the blue distributions.

2025 JINST 20 P08034

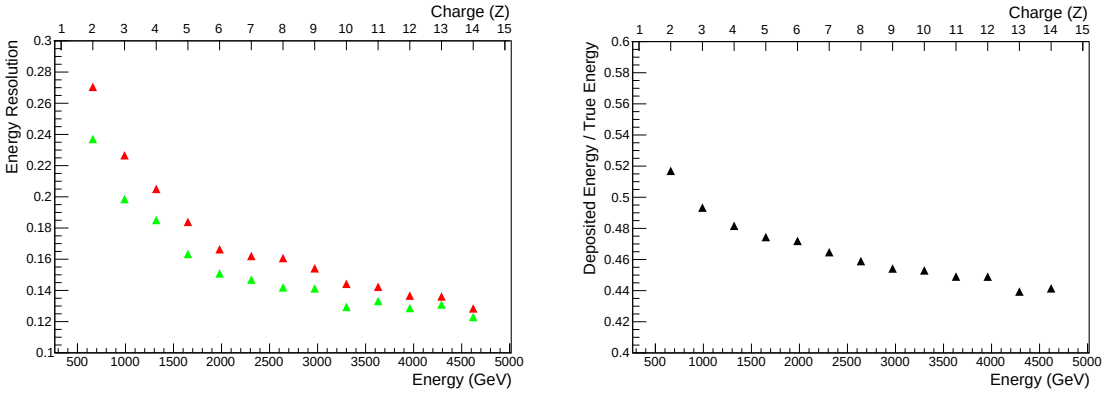

Figure 10. The figure on the left shows the energy resolution for energy measured with the *effective length* correction. Red markers correspond to a sample of all events, while green markers correspond to events with an *effective length* greater than 18 layers. The right figure shows the fraction of energy deposited for all nuclei after the *effective length* correction.

to the variation of the depth of the calorimeter seen by the showers, but the intrinsic fluctuation of the leakage remains also for constant depth. This latter fluctuation is more important for showers with smaller *effective length*, and therefore it is possible to improve the energy resolution by cutting out events with too small value of the *effective length*. Figure 10 reports the energy resolution after *effective length* correction for all events and for a selection of events with more than 18 layers of *effective length*. The energy resolution values are compatible with those expected for HERD like missions [8, 17], thus validating the expected performances. The improvement in resolution due to the selection is visible, but it is not as important as it should be for the whole HERD [8] due to the different distribution of *effective length* already discussed in this paragraph. The improvement in energy resolution with increasing atomic number is mainly due to the superposition of showers induced by each nucleon, which reduces overall fluctuations. Finally, the right plot in figure 10 shows the dependence of the fraction of energy deposited (including the *effective length* correction) on the charge of the nucleus. As the atomic weight increases at fixed value of energy/particle, the shower is expected to shrink and the longitudinal energy leakage to decrease, but the opposite effects are expected for increasing energy, the net results here is a decrease in the fraction of energy deposited in the prototype CALO with increasing atomic number.

5 Conclusions

The response of a large scale calorimeter prototype of the HERD project to high energy nuclei has been studied using data collected at the CERN-SPS accelerator at energies of $330 \cdot Z$ (GeV).

The tested prototype, read out by the photo-diodes system, had a depth of $2.94\lambda_i$ along the beam, which is close to that foreseen for HERD. The data analysis focused on the reconstruction of the first interaction point, which allows the determination of the *effective length* seen by the showers. The energy deposition of nuclei from $Z = 2$ to $Z = 14$ is then analyzed in correlation with the *effective length* and calibration curves useful for the HERD mission are computed. The performances of the prototype calorimeter demonstrate the capability of the HERD apparatus to reveal the energy of nuclei with resolutions well below 20% for $Z > 4$.

2025 JINST 20 P08034

Acknowledgments

INFN authors acknowledge the support of ASI for the INFN activities through the ASI-INFN collaboration agreement n. 2023-8-HH.0.

References

[1] O. Adriani and L. Pacini, *Results from high energy direct measurements and future prospects*, *EPJ Web Conf.* **283** (2023) 02001.

[2] AMS collaboration, *The Alpha Magnetic Spectrometer (AMS) on the international space station: Part II — Results from the first seven years*, *Phys. Rept.* **894** (2021) 1.

[3] Y. Asaoka et al., *Energy calibration of CALET onboard the International Space Station*, *Astropart. Phys.* **91** (2017) 1 [arXiv:1712.01757].

[4] DAMPE collaboration, *The DArk Matter Particle Explorer mission*, *Astropart. Phys.* **95** (2017) 6 [arXiv:1706.08453].

[5] F. Gargano, *The High Energy cosmic-Radiation Detection (HERD) facility on board the Chinese Space Station: hunting for high-energy cosmic rays*, *PoS* **ICRC2021** (2022) 026.

[6] P. Betti, *The HERD experiment: new frontiers in detection of high energy cosmic rays*, *PoS* **TAUP2023** (2024) 142.

[7] L. Fariña et al., *Gamma-ray performance study of the HERD payload*, *PoS* **ICRC2021** (2021) 651.

[8] O. Adriani et al., *CaloCube: An isotropic spaceborne calorimeter for high-energy cosmic rays. Optimization of the detector performance for protons and nuclei*, *Astropart. Phys.* **96** (2017) 11.

[9] O. Adriani et al., *The CaloCube calorimeter for high-energy cosmic-ray measurements in space: performance of a large-scale prototype*, 2021 *JINST* **16** P10024 [arXiv:2110.01561].

[10] O. Adriani et al., *The CaloCube calorimeter for high-energy cosmic-ray measurements in space: Response of a large-scale prototype to protons*, *Nucl. Instrum. Meth. A* **1061** (2024) 169079.

[11] C. Altomare et al., *The Silicon Charge Detector of the High Energy Cosmic Radiation Detection facility*, *PoS* **ICRC2023** (2023) 087.

[12] D. Serini et al., *Characterization of the nuclei identification performances of the plastic scintillator detector prototype for the future HERD satellite experiment*, in the proceedings of the *9th International Workshop on Advances in Sensors and Interfaces*, Bari, Italy, June 08–09 (2023), pp. 184–189 [DOI:10.1109/IWASI58316.2023.10164305].

[13] D. Serini et al., *Nuclei identification performances studies of the Plastic Scintillator Detector (PSD) for the future HERD space mission*, *PoS* **ICRC2023** (2023) 112.

[14] P. Hu et al., *A preliminary simulation study of influence of backsplash on the plastic scintillator detector design in HERD experiment*, *Radiat. Detect. Technol. Methods* **5** (2021) 332.

[15] J.-j. Wango et al., *Feasibility study of cosmic-ray components measurement by using a scintillating fiber tracker in space*, *Radiat. Detect. Technol. Methods* **5** (2021) 389.

[16] X. Liu et al., *Side-On transition radiation detector (TRD) based on THGEM*, *Radiat. Detect. Technol. Methods* **4** (2020) 257.

[17] L. Pacini et al., *Design and expected performances of the large acceptance calorimeter for the HERD space mission*, *PoS* **ICRC2021** (2021) 066.

2025 JINST 20 P08034

[18] O. Adriani et al., *Development of the photo-diode subsystem for the HERD calorimeter double-readout*, 2022 *JINST* **17** P09002 [arXiv:2208.04133].

[19] X. Liu et al., *Double read-out system for the calorimeter of the HERD experiment*, *PoS* **ICRC2023** (2023) 097.

[20] P. Betti et al., *Photodiode Read-Out System for the Calorimeter of the Herd Experiment*, *Instruments* **6** (2022) 33.

[21] P. Betti et al., *Double Photodiode Readout System for the Calorimeter of the HERD Experiment: Challenges and New Horizons in Technology for the Direct Detection of High-Energy Cosmic Rays*, *Instruments* **8** (2024) 5.

[22] O. Adriani et al., *The CALOCUBE project for a space based cosmic ray experiment: design, construction, and first performance of a high granularity calorimeter prototype*, 2019 *JINST* **14** P11004 [arXiv:1910.09784].

[23] V. Bonvicini, G. Orzan, G. Zampa and N. Zampa, *A double-gain, large dynamic range front-end ASIC with A/D conversion for silicon detectors read-out*, *IEEE Trans. Nucl. Sci.* **57** (2010) 2963.

[24] O. Adriani et al., *Development of a high-resolution, high-dynamic-range charge detector for ion beam monitoring*, 2025 *JINST* **20** P01019 [arXiv:2412.13934].

[25] O. Adriani et al., *Performance assessment of the HERD calorimeter with a photo-diode read-out system for high-energy electron beams*, 2025 *JINST* **20** P02015 [arXiv:2410.03274].

2025 JINST 20 P08034